Large-eddy simulation of a full-scale glove box fire

Germain Boyer, Uday Chikkabikkodu, Arnaud Mura, Franck Richard

Large-eddy simulation of a full-scale glove box fire

Germain Boyer[a*], Uday Chikkabikkodu[a,b], Arnaud Mura[b], Franck Richard[b]

[a] Institut de Radioprotection et de Sûreté Nucléaire (IRSN), PSN-RES/SA2I/LIE, Cadarache, St Paul Lez Durance 13115, France

[b] Institut P', CNRS - Université de Poitiers - ISAE-ENSMA, POITIERS CEDEX 9 86073, France

[*] Corresponding author

Highlights

- Reactive LES of glove box fire are carried out with prescribed boundary conditions
- A generalized (i.e., multi-fuel) eddy-dissipation model is used to describe combustion
- Solutions obtained with increased levels of resolution display similar levels of heat release
- Increased levels of refinement improve the description of the reactive flow
- The internal flow topology and dynamics of a glove box fire are revealed by these LES

Abstract

Reactive large-eddy simulations (LES) of the stage of peak heat release rate of open atmosphere glove box fires are carried out. To the best of the authors' knowledge, this is the first time that the LES of such a geometry is reported in the literature. A multi-fuel extension of the eddy-dissipation model (EDM) is used to simulate the combustion of the two distinct solid fuels, PMMA and Polycarbonate, relevant to this configuration. Three increasingly refined grids are considered. All of them lead to temperature values that are in good agreement with experimental data, and similar levels of heat release are obtained inside the glove box. From a more quantitative point of view, only the most refined grid leads to satisfactory values of LES quality criteria. The intermediate grid allows resolving a fraction of the inertial range dynamics, while the solution obtained on the coarsest grid exhibits very large turbulent structures with characteristic sizes of the order of the integral length scale. The analysis confirms that the choice of the grid cell size has a significant influence on the description of the local flow hydrodynamics, the location and thickness of the reactive zones. Finally, the simulation results lead to an improved understanding of the reactive flow development and emergence of large heat release rate at the considered critical stage of a glove box fire.

Keywords : Glove box fires; fluid dynamics; reactive large-eddy simulation; heat transfer; grid sensitivity analysis

Nomenclature

Latin letters

$\mathcal{C}$	:	postprocessing cutline
C_{EDM}	:	constant of the Magnussen model
C_K	:	Kolmogorov constant
c_p	:	specific heat capacity
C_w	:	constant of the WALE model
F	:	fuel chemical species
H_b	:	height of the glove box
h	:	specific enthalpy of the mixture
I	:	radiative intensity
I	:	inert chemical species
IQ_k	:	Pope LES quality index
IQ_η	:	Celik LES quality index
j	:	mass flux
L_b	:	width of the glove box
l_b	:	depth of the glove box
l_t	:	turbulence integral length scale
$\mathcal{M}_i$	:	computational grid i with $i = 0, 1, 2$
$\dot{m}$	:	mass flow rate
O	:	oxidiser chemical species
p	:	hydrodynamic component of the pressure field
P	:	thermodynamic component of the pressure field
P	:	product chemical species
$\mathcal{P}$	:	postprocessing cutplane
Pr	:	Prandtl number
Pr_s	:	SGS turbulent Prandtl number
Q	:	second invariant of the VGT
$\dot{q}$	:	heat release rate (HRR)
$\mathcal{S}$	:	postprocessing probe
S	:	deformation tensor
S^d	:	deviatoric part of S
Sc	:	Schmidt number
Sc_s	:	turbulent (SGS) Schmidt number
s	:	mass stoichiometric coefficient or direction coordinate
T	:	temperature
t	:	time
$u_i = (u, v, w)$	:	velocity components
W	:	molar mass

$x_i = (x, y, z)$: spatial coordinates
Y_α : mass fraction of chemical species α
Z : Shvab-Zeldovich variable

Subscripts and superscripts

0 : related to the reference state
m : related to molecular contribution
s : related to SGS contribution
v : related to viscous contribution
α : related to chemical species α

Greek letters

α : chemical species
Δ : grid cell size
Δh_f^0 : enthalpy of formation of species α
$\Delta h_{c,\alpha}$: heat of combustion
δ_t : time step
δ_{PMMA} : thickness of the PMMA plates
δ_{PC} : thickness of the PC plates
δ_S : thickness of the stainless steel plates
ε_r : resolved dissipation rate
ε_s : SGS turbulent dissipation rate
η_K : Kolmogorov length scale
κ : total radiative absorption
κ_g : gas radiative absorption
κ_s : soot radiative absorption
μ : molecular (dynamic) viscosity
μ_s : SGS viscosity
ν : molar stoichiometric coefficient
ρ : density of the mixture
σ : Stefan-Boltzmann constant
τ_v : viscous stress tensor
τ_s : SGS stress tensor
ϕ_t : conductive thermal flux
ϕ_s : SGS thermal flux
ϕ_r : radiative flux
$\dot{\omega}_\alpha$: chemical production rate of species α

Acronyms

CCRT	:	computing center for research and technology
CEA	:	commissariat à l'énergie atomique
CFL	:	Courant Friedrichs Lewy
CPU	:	central processing unit
EDM	:	eddy-dissipation model
GB	:	glove box
GENCI	:	grand équipement national de calcul intensif
HPC	:	high-performance computing
HRR	:	heat release rate
IRSN	:	institut de radioprotection et de sûreté nucléaire
JANAF	:	joint army-navy-air force
LES	:	large-eddy simulation
MAC	:	marker and cell
MMA	:	methyl methacrylate
PC	:	polycarbonate
PMMA	:	polymethyl methacrylate
QUICK	:	quadratic upstream interpolation for convective kinematics
RTE	:	radiative transfer equation
SGS	:	subgrid-scale
TGCC	:	très grand centre de calcul
VGT	:	velocity gradient tensor
WALE	:	wall-adapting local eddy
WSGG	:	weighted sum of grey gases

Operators

$\overline{q}$	:	filtered value of quantity q
$\widetilde{q}$	:	Favre-filtered value of quantity q

1. Introduction and general context

Since the early development of the nuclear industry in the 1950's, several fire incidents involving glove boxes (GBs) have been recorded in nuclear material processing plants: 24 fires in laboratories operated by the United States Atomic Energy Commission between 1956 and 1965 [1], three major accidents at the Rocky Flats site in 1957, 1969, and 2003, with some of them leading to plutonium particles emissions into the atmosphere [2, 3], and 14 fire incidents in french nuclear installations between 1970 and 2010, 12 of which led to a loss of integrity. As such, fires in a nuclear installation may result in the release of radioactive material into the environment. Therefore, in an attempt to evaluate the radiological consequences of fires on the environment and population, fire source terms (i.e., total heat release, pollutant emission, etc.) must be estimated.

For this reason, the French Nuclear Safety Institute (Institut de Radioprotection et de Sûreté Nucléaire, IRSN) has launched several research programs, including the FIGARO program [4], aimed at assessing the kinetics of glove box fires and the resulting risk of release of radioactive matter. Glove box fire experiments were first carried out on real scale 1 m^3 boxes in open atmosphere and in mechanically ventilated conditions in the framework of the BAG CSS campaign [5]. Several configurations of glove boxes with different combinations of Lexan (Polycarbonate, PC) panels and stainless steel panels for the internal box sides were considered. The two biological protections, usually made of Kyowaglas, were replaced by Polymethyl Methacrylate (PMMA) panels in order to avoid exposure to lead. In particular, a reference configuration with two PC panels facing the PMMA panels and all the remaining panels made of stainless steel, used in the BAG CSS 1.2, 1.5, 1.6, and 1.7 tests carried out in open atmosphere, exhibited a critical stage of maximum heat release rate (larger than 3 MW) from 5 to 10 minutes, once the PC panels melted and collapsed on the bottom of the box [5]. This HRR level was significantly larger than those previously obtained with other fire sources featuring a similar calorific load [6]. At this stage, the effective heat of combustion was within the range of the two solid fuels (PMMA and PC) and the combustion efficiency was close to unity. The temperature reached in the centre of the glove box was found to be larger than 1400 K and was seemingly uniform according to measurements obtained from thermocouples mounted at $1/4$, $1/2$, and $3/4$ of the box height. These values were larger than those of the order $1100 - 1200$ K [7] typically observed in buoyant, non-premixed reactive plumes involving heavy, sooty fuels such as PMMA. The possible occurrence of such large heat release rates and temperatures during a glove box fire scenario thus represents a potential threat for the nuclear installations.

In the purpose of assessing the risks associated with this particular stage of maximal HRR observed in the BAG CSS 1.2, 1.5, 1.6, and 1.7 tests, the present contribution aims at describing and analyzing the turbulent reactive flowfield development occurring in these conditions by performing reactive large-eddy simulations (LES) with the CALIF^{3}S-Isis software developed at IRSN. The occurrence of this maximum HRR is closely related to the particular geometry of the glove box holding at this

stage, namely: a skeleton of 4 stainless steel panels; two PMMA panels, the internal and external faces of which are pyrolyzing; and two layers of pyrolysing PC residuals at the bottom of the box, resulting from the collapse of the molten PC panels. The present simulations are carried out at a particular progress of the thermal degradation of the involved solid fuels, so that boundary conditions can be set in terms of prescribed mass flow rates and surface temperatures without simulating the complete pyrolysis process. These boundary conditions are defined according to the total mass loss rate measured in the experiments, the probable structure of the radiative flux arround the box, and the behaviour of PMMA and PC in terms of pyrolysis rates [8, 9]. Recently, reactive LES have successfully managed to describe non-premixed buoyant plumes [10–13] and wall fires [14] which involve the dominant physical phenomena at play in the present case. The corresponding modelling framework, i.e., LES, can therefore be tentatively used, in spite of the restricted set of experimental data available for validation purposes, namely three local temperature measurements performed along the central line of the box. The present set of computations takes advantage of a previous numerical parameterisation retained to proceed with the simulation of a 1 m diameter methane buoyant flame [15] and other canonical cases [14, 16]. Due to the presence of two distinct fuels, such simulations require the introduction of a multi-fuel extension of the original turbulent combustion model of Magnussen [17] based on the infinitely fast chemistry assumption, used so far in CALIF^{3}S-Isis [15, 18] and other fire simulation softwares [13, 19]. In this particular context, the assessment of the numerical simulation results will be obtained, indeed, by comparisons with the available temperature recordings, and also through a detailed analysis of the effects of computational resolution, based on the calculation of the LES quality criteria of Pope [20] and Celik [21] together with spectral analyses of the resolved velocity field , which are applied to three increasingly refined grids.

The present manuscript is organized as follows. In section 2, the main experimental data are presented, and possible choices for the unknown boundary conditions values are discussed in the light of available measurements. In section 3, the computational model – including transport equations, physical modelling and discretisation choices – is described. In section 4, the results obtained with three computational grids featuring increasing levels of refinement are analysed according to (i) the relevance of the simulation with respect to available experimental data (temperature measured inside the box, consistency between imposed mass flow rates and thermal stress recorded at blowing surfaces), (ii) the accuracy of turbulence resolution, (iii) the resulting hydrodynamics and reactive flow structure. Finally, conclusions and perspectives are provided in Section 5.

2. Experimental case

2.1. Description of the glove box and available experimental data

The initial configuration of the glove box considered in the present work is made of four stainless steel panels at the top, bottom, front, and rear sides of the box, and two polycarbonate (PC) panels at the left and right sides containing gloves holes (lower holes) or taps (upper holes). Two PMMA panels are facing the PC panels and are separated from them by an air gap. The glove box and panel dimensions (width L_b, depth l_b, height H_b, glove holes diameters $d_{g,PMMA}$ and $d_{g,PC}$ in the PMMA and PC panels, air gap thickness δ_a, PMMA, PC and stainless steel panels thicknesses δ_{PMMA}, δ_{PC}, and δ_S) are reported in Figure 1. It is noteworthy that the ignition source, applied during the early 4 minutes of the fire scenario, is placed below the right PMMA panel.

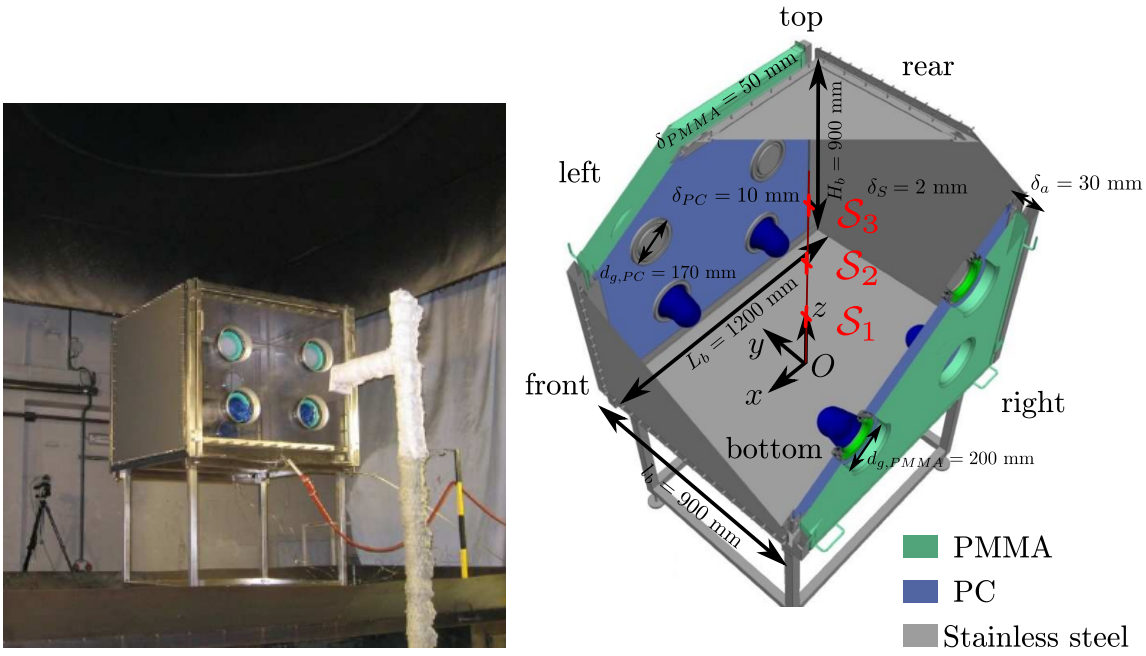

Figure 1: Left: glove box of the BAG CSS 1.2 test in the IRSN Saturne facility. Right: considered experimental glove box configuration and main dimensions. The thermocouple positions $\mathcal{S}_1$, $\mathcal{S}_2$, and $\mathcal{S}_3$ and the coordinates system used in the numerical simulations are reported.

In all the tests of the BAG CSS campaign [5], the following measurements were available amongst others: fire source mass and mass loss rate ($\dot{m}$), exhaust gas measurements including mass flow rate, pressure, oxygen, carbon monoxide, carbon dioxide, and soot concentrations, allowing the estimation of the total HRR (hereafter denoted by $\dot{q}$); temperature measurements using thermocouples located at 225 mm, 450 mm, and 675 mm, respectively, above the origin O of the axis used for this study (positions denoted by $\mathcal{S}_1$, $\mathcal{S}_2$, and $\mathcal{S}_3$ in Figure 1).

The tests were carried out in open atmosphere in the IRSN SATURNE facility. The room of SATURNE facility features large dimensions with an area of 10×10 m^2 and the corresponding

tower has a height of 20 m. It is equipped with a smoke extraction hood of 4.5×4.5 m^2 placed at 3 m above the platform floor. The open atmosphere condition is ensured by air openings located at the top of the tower, which are combined with an extraction system (with a maximum renewal rate of 25000 m^3/h). In the present case, the considered fuel mass flow rate $\dot{m}_F = 0.10$ kg/s corresponds to an oxidizer mass flow rate $\dot{m}_{O,st} = 0.19$ kg/s at stoichiometry. Considering that the extraction system ensures an oxidizer admission rate of $\dot{m}_O = 1.93$ kg/s, the possible effects of air vitiation are considered to be negligible.

The resulting glove box fire scenarios exhibited the same phases of fire propagation, independently from the power of the applied ignition source: i) ignition of the PMMA front panel and subsequent fire propagation; ii) melting and opening of the front gloves and hole plugs; iii) beginning of front PC panel collapse; iv) melting and opening of the rear glove holes; v) end of front PC panel collapse; vi) collapse of the rear PC panel; vii) collapse of the front PMMA panel; and finally viii) collapse of the rear PMMA panel.

Amongst these steps, a period of maximal heat release rate, lasting between 5 and 10 minutes from the collapse of the PC panels to the collapse of the front PMMA panel, was particularly critical. For the BAG CSS 1.2, 1.5, 1.6, and 1.7 tests carried out with the same geometrical configuration [1], this stage was characterized by a mass loss rate $\dot{m} = 0.106$ kg/s and a heat release rate $\dot{q} = 3.16$ MW, in average, during these periods, with 0.003 kg/s and 0.1 MW repeatability deviations. The average temperatures inside the box were $T(S_1) = 1380 \pm 20$ K, $T(S_2) = 1420 \pm 25$ K, and $T(S_3) = 1425 \pm 25$ K.

2.2. Conditions holding at the stage of peak heat release rate

In the absence of direct measurements of the boundary conditions holding at the surface of the glove box panels, a set of consistent boundary conditions, consistent with the global measurements (total mass loss, total heat release rate), must be chosen.

The corresponding values have been estimated considering the known differences that exist – in terms of thermal degradation – between the two main constitutive materials (in terms of calorific loads) of the glove box, namely PMMA and PC. Indeed, both materials have been extensively studied either (i) experimentally, using cone calorimeter and other specific devices, or (ii) numerically using dedicated detailed pyrolysis models.

In particular, self-sustained pyrolysis experiments carried out on 0.25×0.45 m^2 vertical PMMA plates by Pizo *et. al.* [22] are representative of the conditions holding on the external faces of the PMMA panels. The values obtained for the mass loss rate per unit area were of the order of 0.005 kg/m^2/s for a wide range of conditions, so that the total mass flow rate on the external side, i.e.,

[1] All these tests were carried out on the same geometrical configuration. Test BAG CSS 1.7 is a repoductibility test of BAG CSS 1.2. Tests BAG CSS 1.5 and 1.6 were carried out with a different ignition procedure (100 W instead of 50 kW propane burner) but lead to the same fire scenario delayed by roughly 30 minutes due to a longer incubation period.

$\dot{m}_{PMMA,out}$, is of the order of 0.01 kg/s.Then, cone calorimeter experiments carried out on PMMA and PC slabs by Stoliarov *et. al.* [8, 9] provide useful information on the relative orders of magnitude of the pyrolysis mass loss rates per unit area under similar thermal stresses. Indeed, in the case of PMMA and PC samples of similar thicknesses[2] irradiated by a cone heater flux of 75 kW/m^2, PMMA pyrolysis exhibits a quasi-steady threshold value of the order of $\dot{m}''_{PMMA} = 0.032$ kg/m^2/s, whereas the maximal value obtained for PC is of the order of $\dot{m}''_{PC} = 0.012$ kg/m^2/s, suggesting that, in thermal conditions relevant to a fully-developed fire — which are assumed to be reached inside the glove box — the ratio $\dot{m}''_{PC}/\dot{m}''_{PMMA}$ is of the order of $3/8$. As a consequence, assuming that the same thermal flux is applied on the inner surfaces of the PMMA panels and on layers of molten PC deposited onto the bottom of the box, and considering the order of magnitude of the total areas $S_{PMMA,in} = 2L_bH_b$ and $S_{PC} = 2L_bl_b/3$ of the inner blowing surfaces, the ratio between the total mass loss flow rates resulting from the inner PMMA panels and PC layers is of the order of $\dot{m}_{PC}/\dot{m}_{PMMA,in} = S_{PC}\dot{m}''_{PC}/S_{PMMA,in}\dot{m}''_{PMMA} = 1/8$. In these conditions, considering that $\dot{m}_{PMMA,ext} + \dot{m}_{PMMA,in} + \dot{m}_{PC} = 0.1$ kg/s, this leads to the values $\dot{m}_{PMMA,ext} = 0.01$ kg/s, $\dot{m}_{PMMA,in} = 0.08$ kg/s, and $\dot{m}_{PC} = 0.01$ kg/s, which have been used for the purpose of the present study.

Temperatures on the various panels must also be specified as boundary conditions. For the PMMA panels and PC layers, a natural choice is to impose an estimation of the pyrolysis temperatures. For the stainless steel panels, it will be assumed that a thermal convective-radiative equilibrium between the temperature T_{GB} inside the box, the panel temperature T_S and the external ambient temperature ($T_{\text{ref}} = 300$ K) is readily reached. The corresponding equilibrium temperature T_S is approximately equal to 1200 K. Finally, an estimate of the velocity scale in the flow can be useful to provide a preliminary description of mass transfer and turbulence. Introducing a reference macroscopic length scale $D_b = (L_bl_bH_b)^{1/3}$, the velocity $u_{\text{ref}} = \sqrt{2gD_b(T_{\text{GB}} - T_{\text{ref}})/(T_{\text{GB}} + T_{\text{ref}})}$, associated with the transformation of the potential energy of the hot gases in the box into kinetic energy, can be used for this purpose. Its value is about 3.6 m/s. This leads to a Reynolds number value of 10^5, which suggests that centimetric cell sizes used for the simulation of large scale plumes [12, 15], featuring similar Reynolds number values, is a correct initial choice.

3. Numerical model

The present set of reactive large-eddy simulations (LES) is carried out with the version 6.3 of the CALIF^{3}S-Isis software [23], which has been thoroughly validated [24] and widely used [25, 26] for the simulation of non-reactive natural convection flows. It has also successfully reproduced reactive plume flows, e.g., the Mc Caffrey flame [24], and the SANDIA FLAME experiment [15].

[2]These thicknesses are 8.5 mm and 9 mm for PMMA and PC, respectively.

3.1. Governing equations

The considered numerical model is based on the Favre-filtered Navier-Stokes equations written in a low-Mach number formulation. It includes the enthalpy and chemical species mass fractions conservation equations. Let $(x_i) \equiv (x, y, z)$ be the coordinate system, the corresponding set of equations can be written as follows:

$$\frac{\partial \bar{\rho}}{\partial t} + \frac{\partial}{\partial x_i}\left(\bar{\rho}\tilde{u}_i\right) = 0 \tag{1}$$

$$\frac{\partial(\bar{\rho}\tilde{u}_k)}{\partial t} + \frac{\partial}{\partial x_i}\left(\bar{\rho}\tilde{u}_i\tilde{u}_k\right) = -\frac{\partial \bar{p}}{\partial x_k} + \frac{\partial}{\partial x_i}\left(\tau_{v,ik} + \tau_{s,ik}\right) - (\bar{\rho} - \rho_0)g_k \tag{2}$$

$$\frac{\partial(\bar{\rho}\tilde{h})}{\partial t} + \frac{\partial}{\partial x_i}\left(\bar{\rho}\tilde{u}_i\tilde{h}\right) = \frac{\partial}{\partial x_i}\left(\phi_{t,i} + \phi_{s,i} + \phi_{r,i}\right) + \frac{\mathrm{d}P}{\mathrm{d}t} \tag{3}$$

$$\frac{\partial(\bar{\rho}\tilde{Y}_\alpha)}{\partial t} + \frac{\partial}{\partial x_i}\left(\bar{\rho}\tilde{u}_i\tilde{Y}_\alpha\right) = \frac{\partial}{\partial x_i}\left(j_{m,\alpha,i} + j_{s,\alpha,i}\right) + \bar{\dot{\omega}}_\alpha \tag{4}$$

where $\bar{\rho}$ denotes the filtered density, $\tilde{u}_k$ is the Favre-filtered velocity component in direction k, $\tilde{h}$ is the Favre-filtered enthalpy, and $\tilde{Y}_\alpha$ denotes the Favre-filtered mass fraction of chemical species α. The quantity $\bar{p}$ is the filtered value of the dynamic pressure whereas P denotes the thermodynamic contribution of pressure. The value ρ_0 denotes a reference density value (ambient condition) and its local filtered value $\bar{\rho}$ is deduced from the perfect gas law:

$$\bar{\rho} = \frac{PW}{R\tilde{T}}, \quad \frac{1}{W} = \sum_\alpha \frac{\tilde{Y}_\alpha}{W_\alpha} \tag{5}$$

where R is the perfect gas constant, $\tilde{T}$ is the filtered value of the temperature, and W_α are the molar weights of chemical species α.

3.1.1. Turbulence modelling

In Equation (2), the viscous τ_v and subgrid-scale (SGS) stress tensors τ_s are expressed as:

$$\tau_{v,ik} = 2\mu\tilde{S}^d_{ij}, \quad \tau_{s,ik} = 2\mu_s\tilde{S}^d_{ij}, \tag{6}$$

where μ is the temperature-dependent molecular viscosity determined from the Sutherland law, μ_s is the SGS viscosity, and $\tilde{S}^d_{ij} = \tilde{S}_{ij} - \tilde{S}_{kk}\delta_{ij}/3$ is the deviatoric part of the resolved strain-rate tensor $\tilde{S}_{ij} = (\partial\tilde{u}_j/\partial x_i + \partial\tilde{u}_i/\partial x_j)/2$. The quantity μ_s is expressed according to the WALE model [27]:

$$\mu_s = (C_w\Delta)^2 \frac{\left(\tilde{\zeta}_{ij}\tilde{\zeta}_{ij}\right)^{3/2}}{\left(\tilde{S}_{ij}\tilde{S}_{ij}\right)^{5/2} + \left(\tilde{\zeta}_{ij}\tilde{\zeta}_{ij}\right)^{5/4}} \tag{7}$$

where Δ denotes the grid cell size and $\tilde{\xi}_{ij} = (\partial\tilde{u}_k/\partial x_i \cdot \partial\tilde{u}_j/\partial x_k + \partial\tilde{u}_k/\partial x_j \cdot \partial\tilde{u}_i/\partial x_k)/2 - \partial\tilde{u}_l/\partial x_k \cdot \partial\tilde{u}_k/\partial x_l)\delta_{ij}/3$. The WALE model constant C_w is set equal to its usual value, i.e., $C_w = 0.5$.

3.1.2. Heat and mass transfer modelling

In Equation (3), the enthalpy $\tilde{h}$ is expressed as a mass-weighted average of chemical species enthalpies:

$$\tilde{h} = \sum_{\alpha} \tilde{Y}_\alpha h_\alpha(\tilde{T}), \quad h_\alpha(\tilde{T}) = \int_{T_0}^{\tilde{T}} c_{p,\alpha}(\theta)\mathrm{d}\theta + \Delta h^0_{f,\alpha} \tag{8}$$

where $T_0 = 298.15$ K is a reference temperature, and $c_{p,\alpha}$ and $\Delta h^0_{f,\alpha}$ denote the chemical species specific heat capacities and enthalpy of formation. The evolution of the specific heats with temperature $c_{p,\alpha}(T)$ and the enthalpies of formation $\Delta h^0_{f,\alpha}$ of chemical species are extracted from the JANAF database [28].

The conductive thermal flux ϕ_t and molecular mass flux $j_{m,\alpha}$ in Equations (3) and (4) are modelled according to the Fourier and Fick laws, respectively, and, by analogy, their SGS counterparts ϕ_s and $j_{s,\alpha}$ are modeled on the basis of the turbulent diffusivity approximation:

$$\phi_{t,i} = -\frac{\mu}{Pr}\frac{\partial\tilde{h}}{\partial x_i}, \quad \phi_{s,i} = -\frac{\mu_s}{Pr_s}\frac{\partial\tilde{h}}{\partial x_i} \tag{9}$$

$$j_{m,\alpha,i} = -\frac{\mu}{\bar{\rho}Sc}\frac{\partial\tilde{Y}_\alpha}{\partial x_i}, \quad j_{s,\alpha,i} = -\frac{\mu_s}{\bar{\rho}Sc_s}, \frac{\partial\tilde{Y}_\alpha}{\partial x_i} \tag{10}$$

where Pr and Pr_s denote the laminar and SGS turbulent Prandtl numbers and Sc and Sc_s are the laminar and SGS turbulent Schmidt numbers. Here, the equality $Pr = Sc$ is imposed and, in practice, the values $Pr = Sc = 0.7$ and $Pr_s = Sc_s = 0.7$ are used.

Radiative losses are also accounted for in Equation (3), through the filtered radiative flux ϕ_r, estimated by solving the non-spectral radiative transfer equation (RTE) for an absorbing, non-scattering medium. If we denote the radiative intensity by I, depending on the space coordinates x_i and direction coordinates s, the RTE can be expressed as follows:

$$\frac{\mathrm{d}I}{\mathrm{d}s} + \kappa\, I = \frac{\kappa\sigma}{\pi}T^4 \tag{11}$$

where σ denotes the Stefan-Boltzmann constant and κ is the medium absorption coefficient. In the present work, κ includes i) the contribution κ_g of the gaseous combustion products H_2O and CO_2 through the non-spectral weighted sum of grey gases (WSGG) model [29] in which the grid cell size is considered as the absorption path length, and ii) the contribution κ_s of the soot is based on the Novozhilov correlation [30]. At the boundaries, the radiative reflection at the different involved

walls is accounted for by prescribing surface emissivities of 0.85 for PMMA [8], 0.9 for the PC panels [9], and 0.9 for stainless steel panels that are assumed covered with soot.

3.1.3. Combustion modelling

In order to account for the simultaneous combustion of PMMA and PC pyrolysis volatiles, a multi-fuel extension of the eddy-dissipation model [17] is derived. It considers the combustion of a set of N_F fuels $\{F_k\}_{k\in[|1,N_F|]}$ according to single step reactions:

$$\mathsf{F}_k + \nu_{\mathsf{O},k}\mathsf{O} + \sum_n \mathsf{I}_n \rightarrow \sum_p \nu_{\mathsf{P}_p,k}\mathsf{P}_p + \sum_n \mathsf{I}_n \tag{12}$$

where O denotes the oxidizer, $\{\mathsf{I}_n\}_{n\in[|1,N_\mathsf{I}|]}$ is a set of N_I inert species, $\{\mathsf{P}_p\}_{p\in[|1,N_\mathsf{P}|]}$ a set of N_P combustion products, and $\nu_{\mathsf{O},k}$ and $\nu_{\mathsf{P}_p,k}$ are molar stoichiometric coefficients. Each reaction is associated with a reaction rate $\bar{\tilde{\omega}}_{\mathsf{F},k}$. Their modelling follows the same basic rules as those described in reference [31], coincides with the original model of Magnussen [17] for a single fuel, and ensures $\bar{\tilde{\omega}}_{\mathsf{F},k} \rightarrow 0$ as $\tilde{Y}_{\mathsf{F}_k} \rightarrow 0$ and $\tilde{Y}_\mathsf{O} \rightarrow 0$:

$$\bar{\tilde{\omega}}_{F,k} = -\frac{C_{\mathrm{EDM}}\mu_s}{\Delta^2 Sc_s}\tilde{Y}_{\mathsf{F}_k}\frac{\min\left(\sum_{l=1}^{N_\mathsf{F}} s_l\tilde{Y}_{\mathsf{F}_l}, \tilde{Y}_\mathsf{O}\right)}{\sum_{l=1}^{N_\mathsf{F}} s_l\tilde{Y}_{\mathsf{F}_l}} \tag{13}$$

$$= -\frac{C_{\mathrm{EDM}}\mu_s}{\Delta^2 Sc_s}\tilde{Y}_{\mathsf{F}_k}\frac{\left(\sum_{l=1}^{N_\mathsf{F}} s_l\tilde{Y}_{\mathsf{F}_l} + \min(0,-\tilde{Z})\right)}{\sum_{l=1}^{N_\mathsf{F}} s_l\tilde{Y}_{\mathsf{F}_l}} \tag{14}$$

where $C_{\mathrm{EDM}} = 10$ is a calibration constant and $\tilde{Z}$ is a conserved passive scalar that may be thought as the filtered value of a Schwab-Zeldovich variable:

$$\tilde{Z} = \sum_{k=1}^{N_\mathsf{F}} s_k\tilde{Y}_{\mathsf{F}_k} - \tilde{Y}_\mathsf{O} \tag{15}$$

where $s_k = \nu_{\mathsf{O},k}W_{\mathrm{O}_2}/W_{\mathsf{F}_k}$. Accordingly, the set of transport equations (4) is solved as follows: i) The conserved scalar transport equation for $\tilde{Z}$ is solved as a preliminary step; ii) Equations (4) for the fuel subset $\alpha \in \{\mathsf{F}_k\}_{k\in[|1,N_\mathsf{F}|]}$ of chemical species are solved altogether using the second formulation of the reaction rates (13), ensuring the positivity of the fuel mass fractions; iii) $\tilde{Y}_\mathsf{O}$ is deduced from $\tilde{Z}$ and the set of $\tilde{Y}_{\mathsf{F}_k}$ according to Equation (15); iv) Equations (4) are sequentially

Table 1
Molar stoichiometric coefficients (mol/mol) for the combustion of PMMA and PC pyrolysis volatiles

Solid fuel	Pyrolysis volatile	ν_{P}	ν_{P_1}	ν_{P_2}	ν_{P_3}
PMMA	MMA, $C_5H_8O_2$	5.8167	4.0	4.8167	0.2866
PC	Phenol,C_6H_5OH	6.2236	3.0	5.2236	0.7855

solved for $\alpha \in \{\mathsf{P}_p\}_{p\in[|1,N_\mathsf{P}|]}$, with source terms

$$\overline{\dot{\omega}}_{\mathsf{P},p} = -\sum_{k=1}^{N_F} s_{\mathsf{P}_p,k}\overline{\dot{\omega}}_{\mathsf{F},k} \tag{16}$$

where $s_{\mathsf{P}_p,k} = \nu_{\mathsf{P}_p,k}W_{\mathsf{P}_k}/W_{\mathsf{F}_k}$. Finally, Equations (4) are sequentially solved for $\alpha \in \{\mathtt{I}_n\}_{n\in[|1,N_\mathtt{I}|]}$.
In practice, the multicomponent reactive system described above is written for the two fuels: Methyl Methacrylate (MMA, $C_5H_8O_2$), the monomer associated to the pyrolysis of PMMA, denoted by F_1, and Phenol ($C_6H_5(OH)$), which is the main pyrolysis product of the PC decomposition [32], denoted by F_2. The single inert species is Nitrogen ($\mathtt{I} \equiv N_2$). The considered combustion products are $\mathsf{P}_1 \equiv H_2O$, $\mathsf{P}_2 \equiv CO_2$, and soot ($\mathsf{P}_3 \equiv C$). The molar stœchiometric coefficients involved in the combustion reactions (12) are adapted from the values obtained for complete combustion to account for soot production in the combustion process. According to Ref. [33], the mass soot yields associated with the combustion of PMMA and PC are 0.022 and 0.112, respectively. The molar coefficients reported in Table 1 are based on these values.

3.2. Computational domain and discretization

The computational domain and the boundaries nomenclature used in the present work is depicted in Figure 2. We consider the maximum-heat-release stage of the fire scenario where the PC panels have melt down on the left and right parts of the glove box. As such, layers of molten, pyrolysing PC are assumed to exist on both sides of the bottom panel, with widths equal to one third of the overall panel width. Both PMMA panels are assumed pyrolysing as well, but since most of the combustion occurs inside the box, the heat fluxes applied on the internal sides of the PMMA panels are much larger than those applied on the external sides. Therefore, three classes of boundary conditions are considered in the vicinity of the glove box: Γ_S for the stainless steel panels, $\Gamma_{PMMA,in}$, and $\Gamma_{PMMA,ext}$ for the internal and external sides of the PMMA panels, and Γ_{PC} for the two layers of the bottom side where the pyrolysing PC has melt down. The external boundaries are denoted by Γ_{ext}. Boundaries Γ_{PC}, $\Gamma_{PMMA,in}$, and $\Gamma_{PMMA,ext}$ are considered as blowing walls with temperatures and mass flow rates prescribed according to the preliminary analysis of section 2.2: $T_{p,PC} = 800$ K and $T_{p,PMMA} = 650$ K (pyrolysis temperatures of the corresponding materials), and $\dot{m}_{PC} = 0.01$ kg/s,

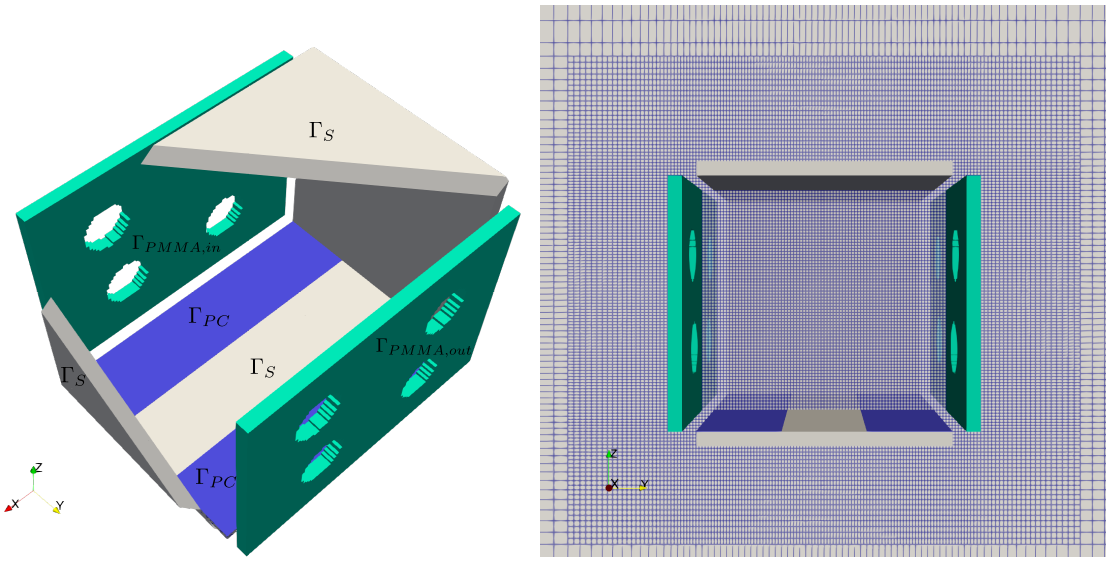

Figure 2: Left: computational domain and nomenclature for the boundary conditions. Right: example of the $\mathcal{M}_1$ grid in the (y, z) plane, obtained with a $n_r = 1$ local cell refinement.

$\dot{m}_{PMMA,in} = 0.08$ kg/s, and $\dot{m}_{PMMA,ext} = 0.01$ kg/s. Similarly, a temperature $T_S = 1200$ K is applied on the faces of the stainless steel panels at thermal equilibrium between the internal box of temperature and the far ambient temperature. On boundary Γ_{ext}, inlet-outlet conditions are applied.

The overall dimensions of the computational domain are $2 \times 2 \times 2.8$ m^3, and the cartesian grids are built in two successive steps: i) a first generic grid is generated with external cell size $\Delta_{ext} = 250$ mm, intermediate size $\Delta_{int} = 50$ mm at a distance $2\Delta_{ext}$ of the glove box, and $\Delta_{GB} = 25$ mm at the surface of the panels and inside the box. This way, the zone of interest including the vicinity of the panels and the inner part of the glove box is discretized with a uniform grid cell size, the remaining part of the computational domain being a buffer zone. ii) It is then possible to locally refine a zone encompassing the box by a $2\Delta_{ext}$ sub-domain, with a refined cell size $\Delta_{GB,r} = \Delta_{GB}/2^{n_r}$, where n_r is the level of local refinement. When local refinement is used, Equations (1-4) are solved on the refined grid, but the RTE (11) is solved on the grid obtained at the first step, without any local refinement. Three different grids — $\mathcal{M}_0$, $\mathcal{M}_1$, and $\mathcal{M}_2$ — obtained with local refinements of level $n_r = 0$, 1, and 2, are used in the present work in order to analyse the dependence of the numerical model to the level of computational resolution. Their reference cell size in the domain of interest $\Delta_{GB,r}$ are of 25 mm, 12.5 mm and 6.5 mm; they feature 0.65, 3.26 and 18.5 million cells, respectively.

The partial differential equations (1-4) are discretized according to a Marker And Cell (MAC) staggered finite volume scheme (normal velocity components expressed at face centers, scalar quantities expressed at the cell centers) [34]. They are sequentially solved using a fractional step algorithm. The coupled mass-momentum problem is thus solved using a fractional step scheme

through a pressure correction method [35]. For the momentum equation, the time derivative is approximated by a semi-implicit second-order Crank-Nicolson scheme, the convective operator is approximated by a discrete kinetic-energy preserving second-order centered scheme [35], and the viscous stress tensor is approximated by second-order finite differences. The discretized mass balance is then used to solve for the scalars conservation equations, with convective and diffusive operators approximated by a third-order QUICK scheme and second-order finite differences, respectively. This combination of discrete operators imposes a CFL constraint on the time step δt. In practice, using the reference velocity u_{ref} introduced in section 2.2, the time step is chosen as $\delta t = 0.1\Delta_{GB,r}/u_{\text{ref}}$ to ensure the stability of the time integration. All these conservation equations are solved within a parallel computing framework with domain splitting performed using the METIS library. The RTE is solved with a finite volume (FV) method [36], with 128 sectors retained for the angular discretization, and the resolution in the different angular sectors split over the available processors. The simulations are carried out in two steps: a 10 s transient is computed using an implicit version of the QUICK scheme for the convective scalar terms discretisation, so that the CFL constraint can be relaxed. Then, the simulation is restarted until the statistical averages — hereafter denoted by angle bracket symbols $\langle\cdot\rangle$ — of the velocity, temperature and mass fractions are converged up to 1%. Simulations with $\mathcal{M}_0$, $\mathcal{M}_1$, and $\mathcal{M}_2$ are run in parallel with 60, 384 and 800 processors on the Irene supercomputer hosted by the CCRT (Computing Center for Research and Technology) of the French Alternative Energies and Atomic Energy Commission (CEA). The corresponding runs require a CPU cost of 370, 2280, and 36800 hours·cores for 10500, 21000, and 42000 iterations.

4. Results and discussion

For the sake of clarity, the planes, cutlines, and local positions at which the data are displayed in this section are reported in Figure 3. According to the coordinates origin defined in Figure 1, $\mathcal{P}_{x_0}$ and $\mathcal{P}_{x_1}$ are planes extracted in the $\mathbf{e}_x$ direction at $x = x_0 = 0$ and $x = x_1 = L_b/4$ respectively; cutlines $\mathcal{C}^{z_1}_{x_0}$, $\mathcal{C}^{z_2}_{x_0}$, $\mathcal{C}^{z_3}_{x_0}$, $\mathcal{C}^{z_1}_{x_1}$, $\mathcal{C}^{z_2}_{x_1}$, and $\mathcal{C}^{z_3}_{x_1}$ are located at (x_0, z_1), (x_0, z_2), (x_0, z_3), (x_1, z_1), (x_1, z_2), and (x_1, z_3), respectively, with $z_1 = H_b/4$, $z_2 = H_b/2$, and $z_3 = 3H_b/4$. Finally, three sensors $\mathcal{S}_1$, $\mathcal{S}_2$, and $\mathcal{S}_3$ located at $(x, y, z) = (0, 0, z_1), (0, 0, z_2)$ and $(0, 0, z_3)$ are also considered to proceed with comparison against experimental measurements of temperature.

4.1. Turbulence resolution

Two quality criteria IQ_k and IQ_η are commonly used for the analysis of the turbulence resolution in LES [20, 21], based either on the ratio of the resolved to the total (i.e. resolved and subgrid scale) parts of the turbulent kinetic energy (TKE), and on a length scale ratio estimate. In this respect, the resolved turbulent kinetic energy $k_{t,r}$ is directly deduced from the resolved velocity field ($k_{t,r} \equiv \langle\tilde{u}_i\tilde{u}_i\rangle/2$) whereas the resolved and SGS dissipation contributions are deduced from

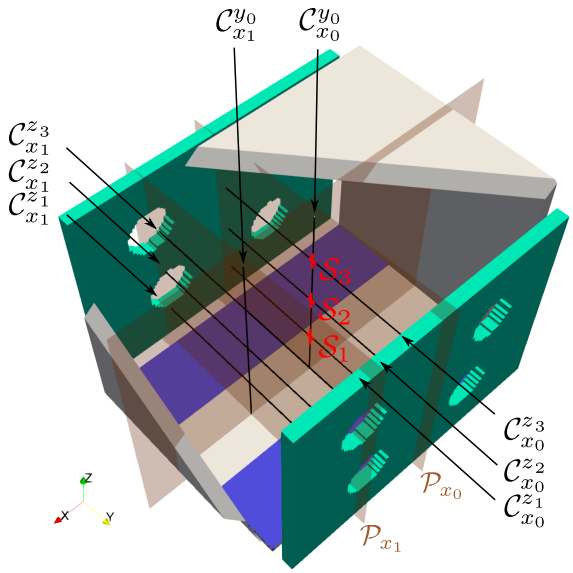

Figure 3: Planes, cutlines and sensors considered for the numerical data analysis.

both laminar and SGS viscosities and resolved velocity field [37]: $\varepsilon_r = \langle 2\mu/\bar{\rho}\tilde{S}^d_{ij}\tilde{S}^d_{ij}\rangle$ and $\varepsilon_s = \langle 2\mu_s/\bar{\rho}\tilde{S}^d_{ij}\tilde{S}^d_{ij}\rangle$. This last quantity is used to estimate the SGS turbulent kinetic energy according to $k_{t,s} = 3C_K(\varepsilon_s\Delta/\pi)^{2/3}$, where $C_K = 1.5$ is the Kolmogorov constant. Using these quantities, the IQ_k and IQ_η quality indexes [20, 21] are defined as:

$$IQ_k = \frac{k_{t,r}}{k_{t,r} + k_{t,s}}, \quad IQ_\eta = \frac{1}{(1 + 0.05\sqrt{\Delta/\eta_K})} \tag{17}$$

where $\eta_K = (\nu^3/\varepsilon)^{1/4}$ is an estimate of the Kolmogorov length scale with $\varepsilon = \varepsilon_r + \varepsilon_s$ an estimate of the total turbulent dissipation. According to reference [20], a LES is sufficiently resolved provided that at least 80% of the turbulent kinetic energy is resolved, i.e., $IQ_k \geq 0.8$, whereas the simulation reaches the DNS limit for $IQ_\eta \geq 0.95$ [38].

Keeping in mind that the Reynolds number value remains rather moderate in buoyant flows, both criteria are investigated here. Plots along cutlines $\mathcal{C}^{y_0}_{x_0}$, $\mathcal{C}^{z_1}_{x_0}$, $\mathcal{C}^{z_2}_{x_0}$, $\mathcal{C}^{z_3}_{x_0}$, $\mathcal{C}^{y_0}_{x_1}$, $\mathcal{C}^{z_1}_{x_1}$, $\mathcal{C}^{z_2}_{x_1}$, and $\mathcal{C}^{z_3}_{x_1}$ are depicted in Figures 4. Surprisingly, grid $\mathcal{M}_0$ allows resolving more than 80% of the turbulent kinetic energy at least in the central part of the box. This ratio is stabilized up to at least 92% for $\mathcal{M}_1$ and $\mathcal{M}_2$ with minor differences. It only decreases in the external zones of plane $\mathcal{P}_{x_1}$ (cutlines $\mathcal{C}^{z_1}_{x_1}$, $\mathcal{C}^{z_2}_{x_1}$, and $\mathcal{C}^{z_3}_{x_1}$) with values that nevertheless remain larger than 0.8 for $\mathcal{M}_1$ and $\mathcal{M}_2$. The value of IQ_η appears to be more discriminant: it ranges between 0.6 and 0.7 for $\mathcal{M}_0$, which clearly indicates an under-resolved solution; it then grows up to nearly uniform values of around 0.75 (i.e., with Δ of the order of $45\eta_K$) for $\mathcal{M}_1$ and 0.8 for $\mathcal{M}_2$, so that the corresponding solution can be considered to be acceptable, $\mathcal{M}_1$ being however slightly under-resolved according to this criterion. At this level, it must be

emphasized that indexes IQ_k and IQ_η (and especially the latter, i.e., IQ_η) have been introduced on the basis of a fully-developed turbulence framework and without any specific account of the possible influence of walls. In this respect, it must acknowledged that, in the direct vicinity of walls, other quantities could be more relevant to assess the resolution quality. For instance, subgrid-scale (SGS) to molecular viscosity ratio values and velocity profiles (in wall units) were previously considered in references [38, 39]. Therefore, the analysis of these indexes should be restricted to the flow region that excludes the closest vicinity of the walls.

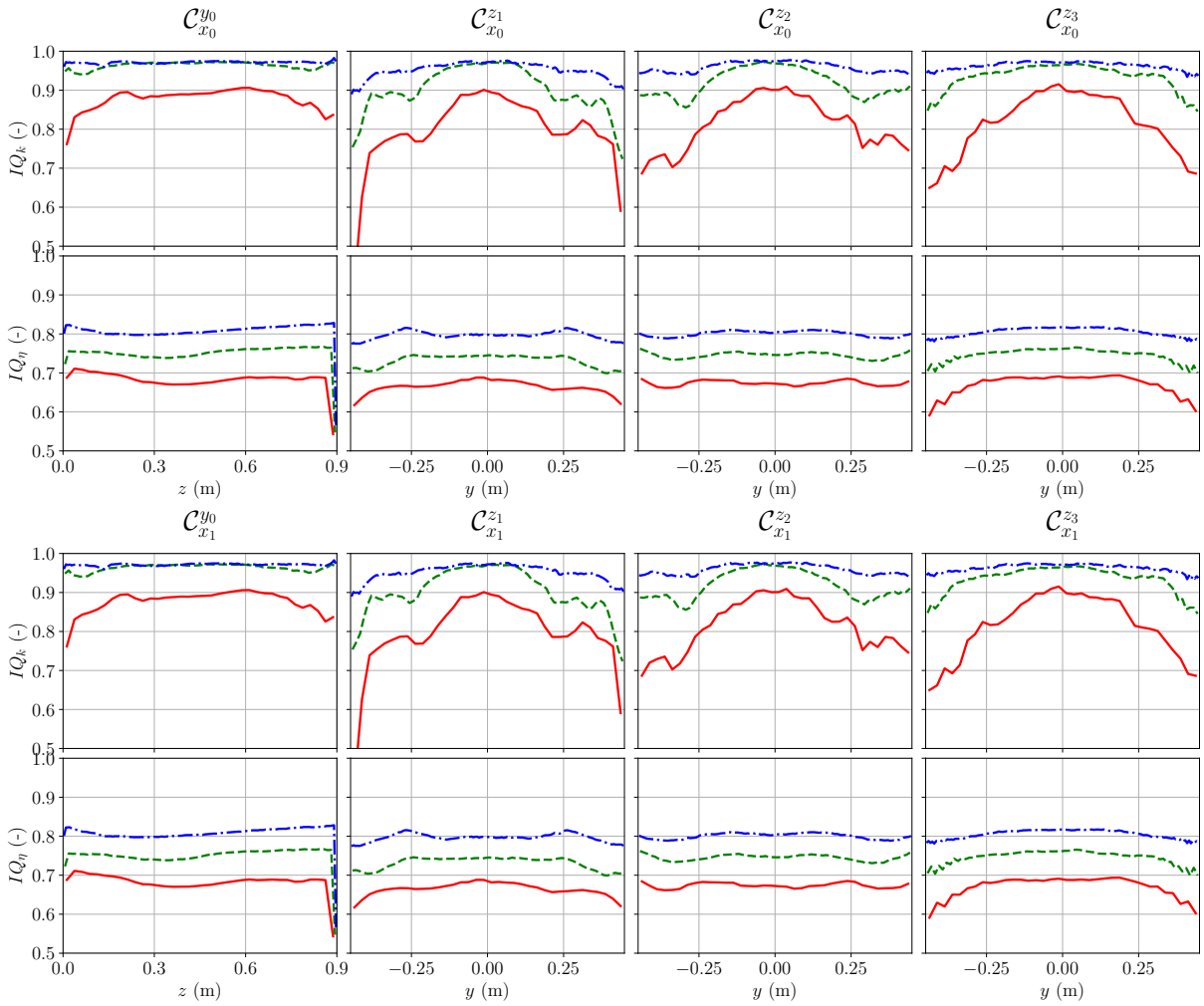

Figure 4: Cutlines of the LES quality criteria IQ_k and IQ_η. —: $\mathcal{M}_0$; – – –: $\mathcal{M}_1$; – · –: $\mathcal{M}_2$.

The resolution quality can be further investigated by considering the Fourier analysis of the temporal recordings of the vertical component of the velocity, computed at locations $\mathcal{S}_1$, $\mathcal{S}_2$, and $\mathcal{S}_3$ (central axis of the box), as reported in Figure 5. Clearly, a $-5/3$ decay rate — which would be relevant to the resolution of the inertial range — does not appear with grid $\mathcal{M}_0$. Only turbulent motions with frequencies smaller than 5 Hz carry a noticeable amount of kinetic energy. In this respect, the

estimation of the integral time scale τ_t such as $1/\tau_t = u_{\text{ref}}/l_t$ is of the order of 1 Hz, associated with the integral length scale $l_t = D_b$, where D_b is the box volume length scale, and the reference velocity u_{ref} is of the order of 1 m/s, this indicates that only motions of size close to the integral length scale are resolved. On the contrary, the Fourier spectra computed for grids $\mathcal{M}_1$ and $\mathcal{M}_2$ exhibit a non-negligible region featuring a $f^{-5/3}$ decay characteristic of the inertial range, before sharper decays in the vicinity of $f = 40$ Hz and $f = 50$ Hz, respectively, associated with the LES cutoff. These results confirm that these two grids are acceptable in terms of required levels of computational resolution.

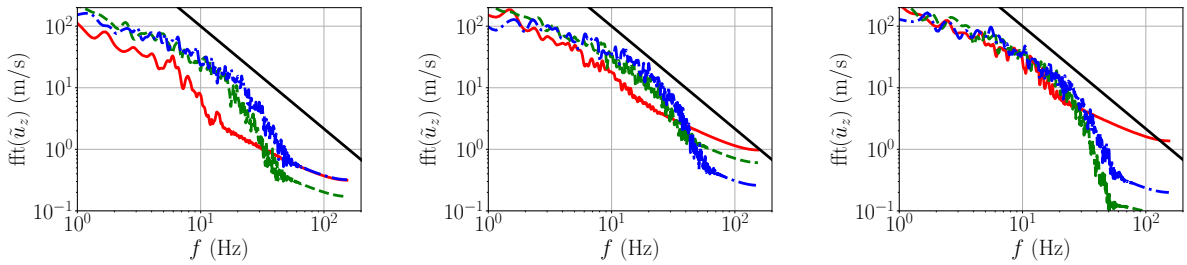

Figure 5: Fourier transforms of instantaneous temporal signals recorded at locations $\mathcal{S}_1$, $\mathcal{S}_2$, and $\mathcal{S}_3$. —: $\mathcal{M}_0$; – – –: $\mathcal{M}_1$; – · –: $\mathcal{M}_2$; (—): $\propto f^{-5/3}$ decay.

4.2. Flow description

The flow dynamics is analysed by considering the instantaneous temperature, velocity, Q-criterion and reaction rates, plotted in the $\mathcal{P}_{x_0}$ and $\mathcal{P}_{x_1}$ planes, as depicted in Figures 6 and 7. Apart from the grid refinement, the joint analysis of the second invariant Q of the velocity gradient tensor (VGT) and velocity fields in both planes suggests the existence of two kinds of resolved vortical structures. The first includes two large structures – featuring $|\nabla \times u|$ of the order of 10 s^{-1} according to the velocity field – which are centred near the PMMA panel between the glove holes. In plane $\mathcal{P}_{x_1}$, they involve the entrainment of fresh external air – as suggested by the temperature fields – through the lower glove holes and the ejection of burnt gases through the upper ones. They are also visible – with less strength – in plane $\mathcal{P}_{x_0}$ in the absence of glove holes, so that the gas entrainment and ejection occurs through the air gaps. These structures are mainly driven by natural convection, insofar as the release of heat in the box induces a rising current that is necessarily associated with the upper ejection of hot gases and the lower entrainment of external gases. It is also worth noticing the occurrence, in $\mathcal{M}_1$ and $\mathcal{M}_2$ only, of two symmetrical structures in the vicinity of the PC layers suggesting the development of recirculation zones. The second kind of structures is made up of vortices – featuring $|\nabla \times u|$ of the order of $20 - 30$ s^{-1} according to the Q-criterion field – that develop along the shear layers induced by the external air entrainment through the lower glove holes and air gaps. They are triggered by shear instabilities and coincide with the regions of maximal

temperature and maximal reaction rates that are associated with the combustion of PMMA or PC pyrolysis volatiles.

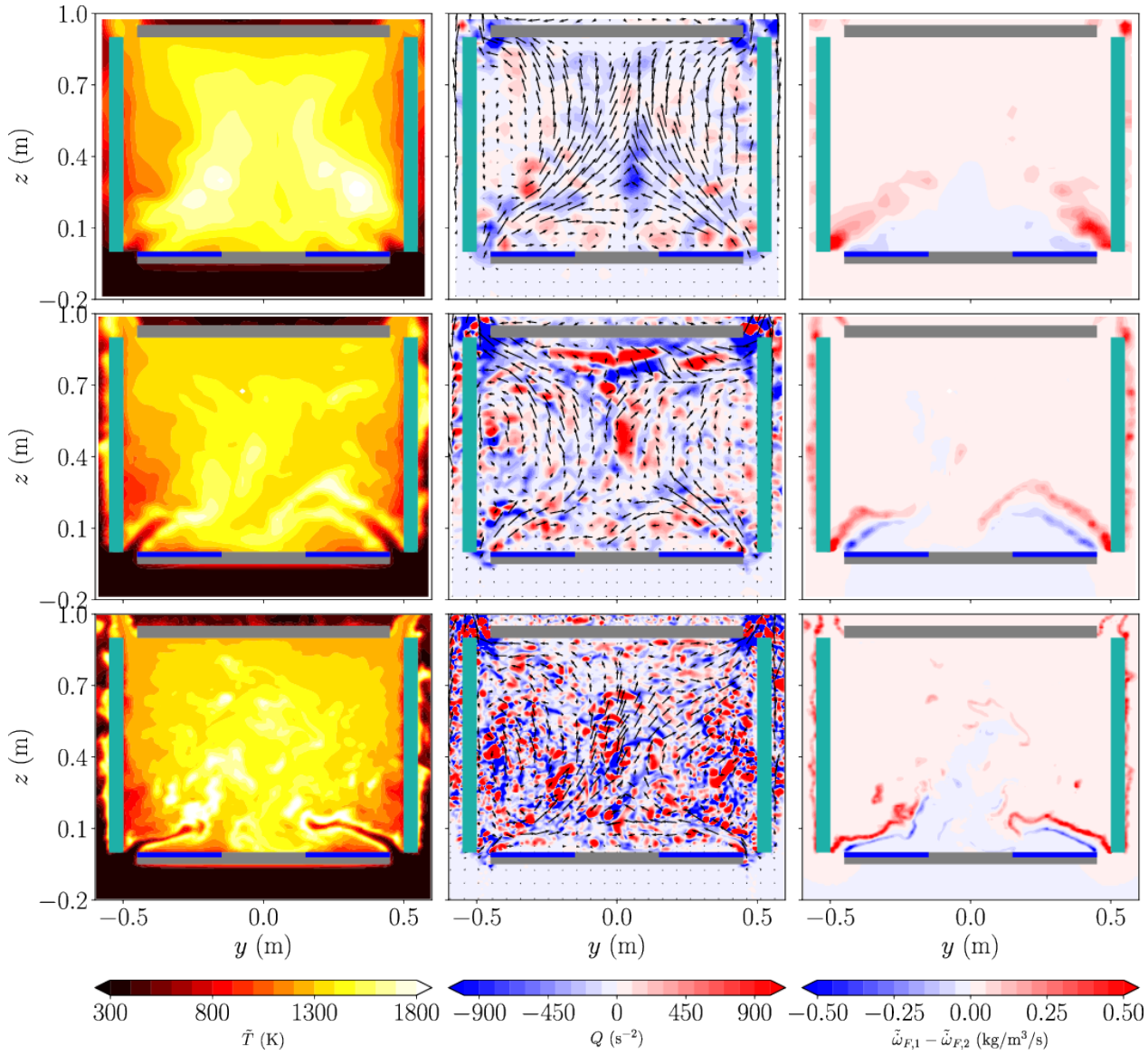

Figure 6: Flowfields snapshots in plane $\mathcal{P}_{x_0}$. Left: temperature; center: second invariant Q of the velocity gradient tensor, and velocity field; right: reaction rates (with positive values for F_1, negative for F_2). Top: grid $\mathcal{M}_0$; middle: grid $\mathcal{M}_1$; bottom: grid $\mathcal{M}_2$. Unsteady visualisations on 2 s of physical time are available as supplementary material.

As a consequence, this flow is characterized by a cyclic coupling between the hydrodynamics of these structures and the heat released within the box through natural convection: the combustion-induced HRR determines the increase of the temperature in the box, and therefore the strength of the vertical convection, and, as a consequence, the entrainment of fresh air that is subsequently consumed in the combustion process. The correct resolution of all these inter-related phenomena is

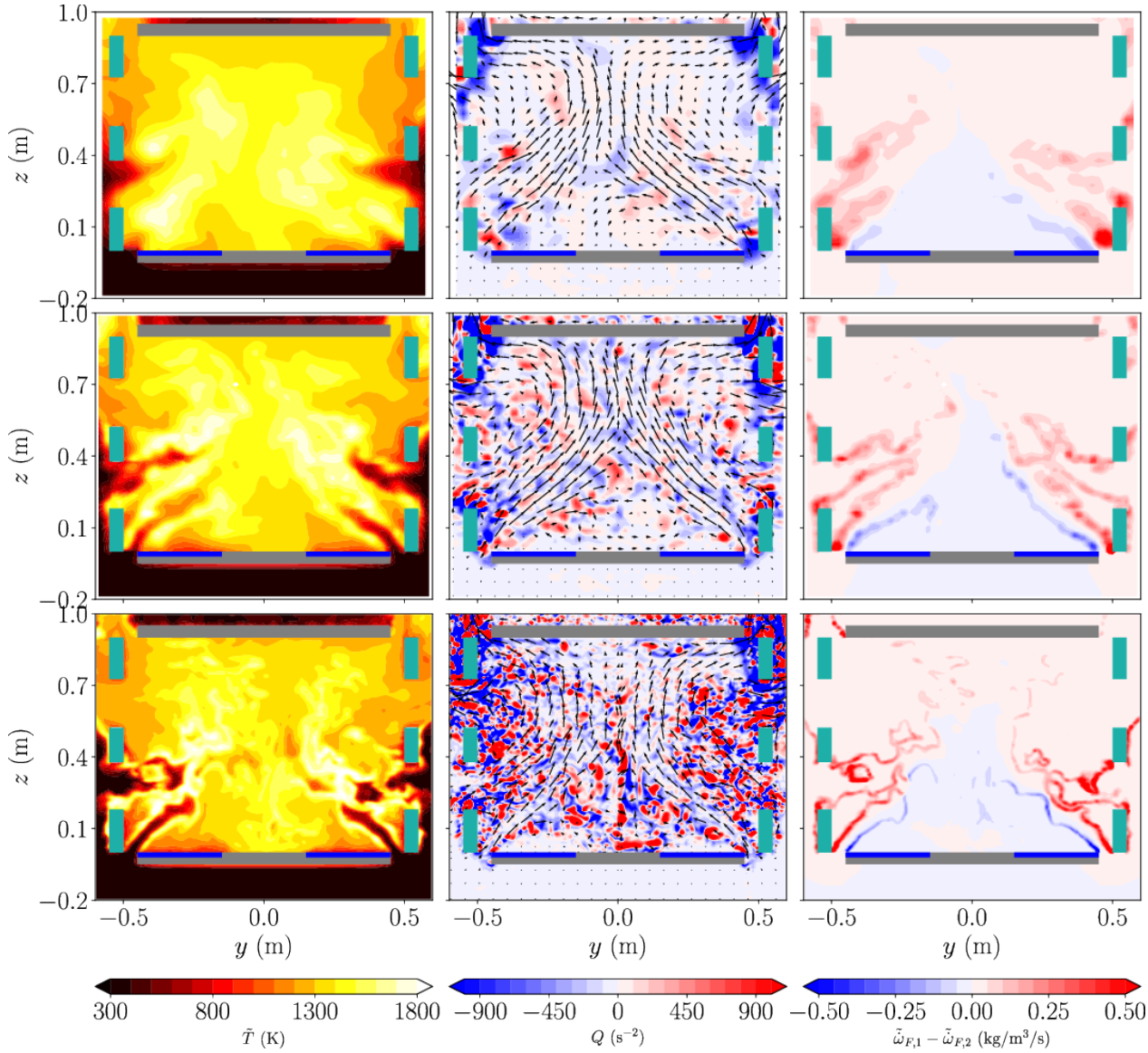

Figure 7: Flowfields snapshots in plane $\mathcal{P}_{x_1}$. Left: temperature; center: second invariant Q of the velocity gradient tensor, and velocity field; right: reaction rates (with positive values for F_1, negative for F_2). Top: grid $\mathcal{M}_0$; middle: grid $\mathcal{M}_1$; bottom: grid $\mathcal{M}_2$. Unsteady visualisations on 2 s of physical time are available as supplmentary material.

far from being straightforward since only the amount of fuels is specified by the boundary conditions, the mass of oxidizer entrained in the box being indeed determined through the resolution of the hydrodynamic structures.

In this respect, increasing the computational resolution has the following effects. The penetration depth of the fresh gases through the lower glove holes and air gaps increases with the grid refinement. According to the cutlines of statistical averages of temperature, ascending velocity, resolved turbulent kinetic energy, and passive scalar mean and variance, depicted in Figures 8 and 9,

the peak temperature and passive scalar variance along the y-axis, which denote the location of maximum reactivity, are stabilized from $y = L_b/4 \approx 0.3$ m with grid $\mathcal{M}_0$ to $y = L_b/6 \approx 0.2$ m with $\mathcal{M}_1$ and $\mathcal{M}_2$ in the lower part of the box (cutline $\mathcal{C}_{x_0}^{z_1}$). It is also worth noticing the much larger values of the passive scalar fraction variance in cutline $\mathcal{C}_{x_0}^{z_1}$ for grid $\mathcal{M}_2$, which suggests a larger unsteady engulfment of fresh gases in this zone. In the vicinity of the lower panel and molten PC layers, only grid $\mathcal{M}_2$ exhibits a maximum of passive scalar mean and variance. The PC volatiles are therefore strongly stirred and the recirculation zone occurring here is destabilized with this grid, which is not reproduced with the coarser ones. Then, the strength of the secondary vortices continuously increases from $\mathcal{M}_0$ to $\mathcal{M}_2$, as suggested by the values of the second invariant Q of the VGT observed in planes $\mathcal{P}_{x_0}$ and $\mathcal{P}_{x_1}$ (Figures 6 and 7). This is associated with different vertical profiles of resolved turbulent kinetic energy: slow increase up to $z \approx H/2$ with $\mathcal{M}_0$, sharp increase up to $z \approx H_b/3$ with $\mathcal{M}_1$ and $\mathcal{M}_2$, with, surprisingly, a larger increase obtained with $\mathcal{M}_1$. According to the instantaneous snapshots (Figures 6 and 7), the reaction zones, that are concentrated in shear layers where these vortices are convected, exhibit a decreasing thickness for increasingly refined grids, so that they clearly decay to reaction sheets with $\mathcal{M}_2$. In summary, the increase of grid refinement may modify the location of the reaction zones. In the perspective of considering large-eddy simulations coupled with the prediction of the fuel mass flow rates, this may affect the local heat flux received by the blowing panels.

However, some important features of the flowfield are reproduced in a similar way with all grids. For PMMA, the peak reactivity occurs near $y = l_b/4$ in these rich zones and $y = 3l_b/8$ in the lower part of plane $\mathcal{P}_{x_1}$, where fresh air enters in non-negligible amounts. For PC volatiles, the reactivity remains noticeable up to $z = H_b/3$, which is far from the location of their injection. In regard to the vertical velocity component, it is negative below $z < H_b/4$, and positive above, which suggests again the presence of a recirculation zone in the lower part of the box. As expected from the experimental data, the average temperature is uniform (around 1400 K) on the central box vertical cutline $\mathcal{C}_{x_0}^{y_0}$, but also on the lateral one $\mathcal{C}_{x_1}^{y_0}$. It remains within the $1300-1500$ K range almost everywhere, except near the (relatively cooler) blowing walls, and in the vicinity of $y = l_b/4$ in the $\mathcal{C}_{x_0}^{z_1}$ cutline where fresh oxidizer, identified by negative values of $\widetilde{Z}$, penetrates through the lower glove holes in plane $\mathcal{P}_{x_1}$. This hot atmosphere is also rich since values $\widetilde{Z}$ exceeds its stoichiometric value Z_{st}. Concerning the experimental data, the temperatures values measured at sensors $\mathcal{S}_1$, $\mathcal{S}_2$, and $\mathcal{S}_3$ are reported together with the computed ones, corrected accounting for the properties of the type-K chromel-alumel thermocouples (diameter 1.5 mm) used in the experiments [40]. Similar values $T(\mathcal{S}_1) = 1455 \pm 20$ K, $T(\mathcal{S}_2) = 1465 \pm 10$ K and $T(\mathcal{S}_3) = 1436 \pm 5$ K are obtained with the three considered grids. These values are slightly overestimated (less than 5%) in comparison with the experimental ones, and are significantly larger than maximal temperature values observed in buoyant reactive plumes involving PMMA, which range between 1100 K and 1200 K [7].

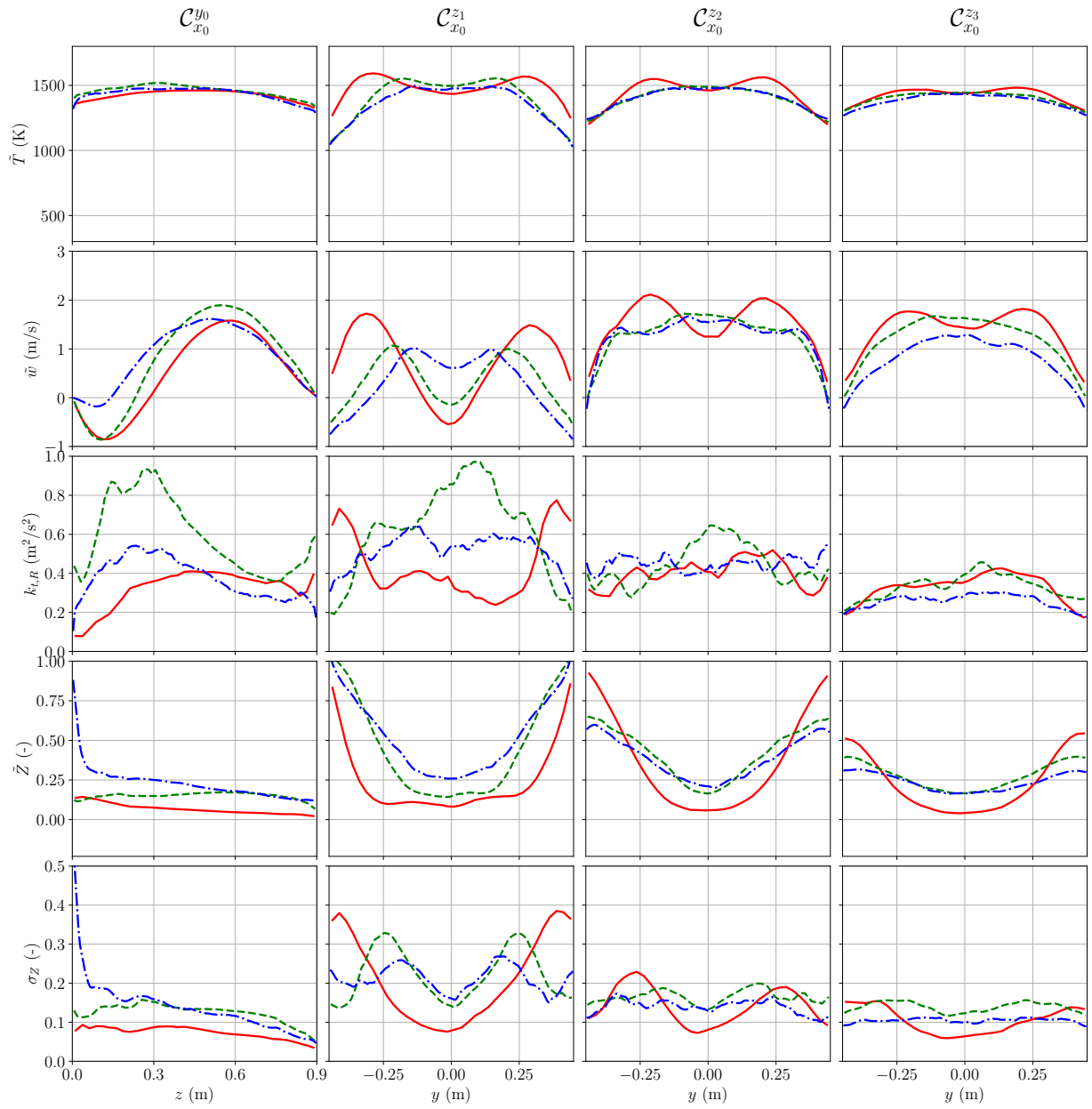

Figure 8: Cutlines in plane $\mathcal{P}_{x_0}$ (mid-distance between the front and rear sides of the box): statistical averages of the filtered temperature, vertical component of velocity, resolved turbulent kinetic energy, passive scalar mean an variance. —: $\mathcal{M}_0$; – – –: $\mathcal{M}_1$; – · –: $\mathcal{M}_2$.

4.3. Global heat balance

Similarly, the integrated amount of fuels burnt inside the box $\dot{m}_{F_k,GB}$, the resulting heat release $\dot{q}_{GB} = \dot{m}_{F_k,GB}\Delta h_{c,F_k}$, and the heat dissipated by radiative transfer $\dot{q}_{r,GB}$ have been calculated. They are reported in Table 3. At this level, it is noteworthy that the resort to the heats of combustion $\Delta h_{c,F_k}$, as evaluated from reference [33], does not take into account possible departures of the

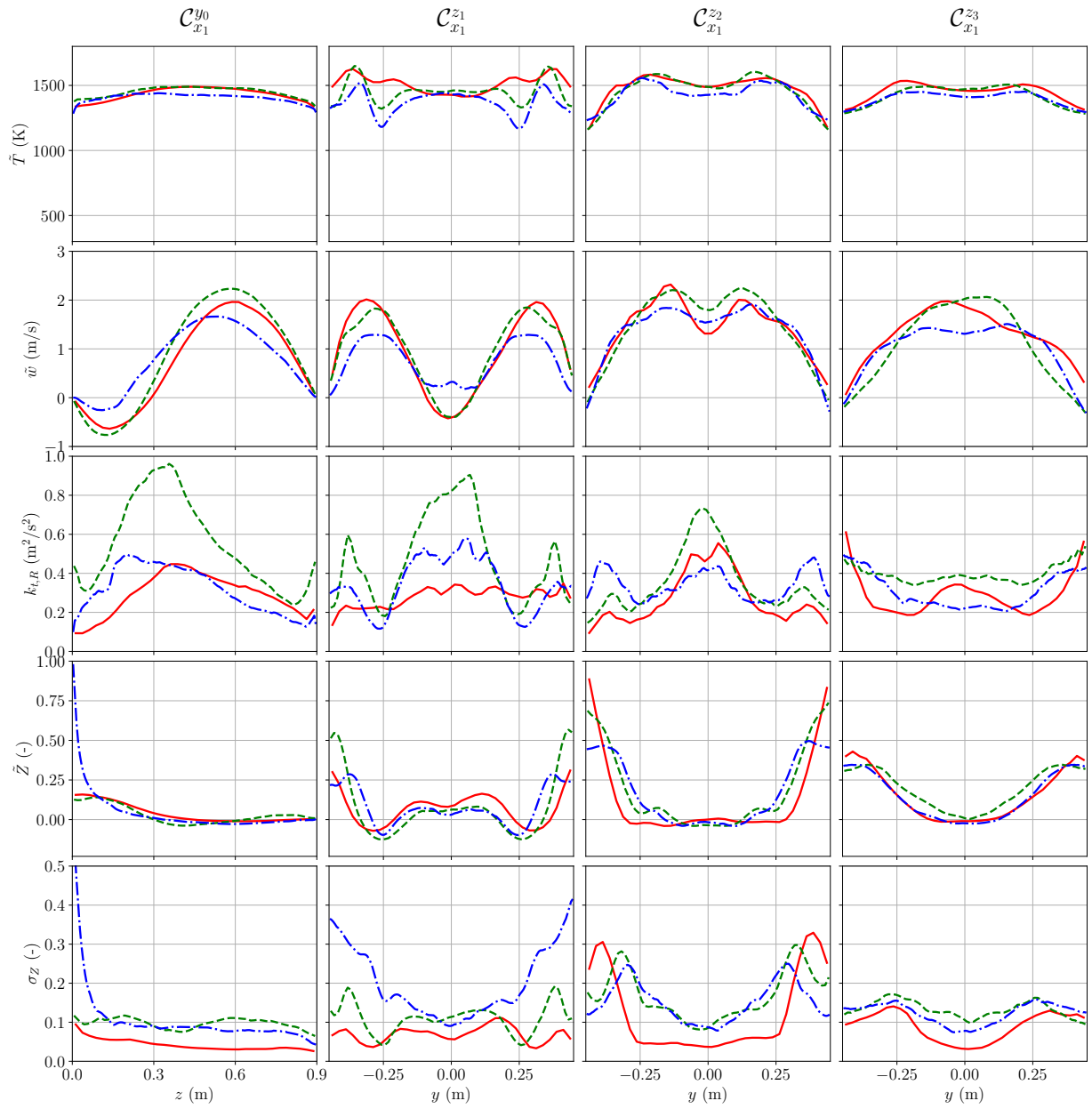

Figure 9: Cutlines in plane $\mathcal{P}_{x_1}$ (quarter-distance between the front and rear sides of the box): statistical averages of the filtered temperature, vertical component of velocity, resolved turbulent kinetic energy, passive scalar mean an variance. —: $\mathcal{M}_0$; – – –: $\mathcal{M}_1$; – · –: $\mathcal{M}_2$.

combustion efficiency from unity. However, it should be emphasized that the objective here is only to proceed with a qualitative comparison between the various simulation results as the mesh cell size is decreased. In this respect, the values reported in Table 3 are rather similar for to the three considered grids: 14% of the PMMA volatiles and 22% of the PC volatiles injected in the box are burnt inside, so that only 14% of the total heat is released inside. This leads us to formulate two

Table 2
Statistical averages of the temperature (K) computed at sensors locations $\mathcal{S}_1$, $\mathcal{S}_2$, and $\mathcal{S}_3$ and comparison with the values averaged over the whole duration of the peak heat release rate stage of tests BAG CSS 1.2, 1.5, 1.6 and 1.7.

	$\langle T(\mathcal{S}_1)\rangle$ (K)	$\langle T(\mathcal{S}_2)\rangle$ (K)	$\langle T(\mathcal{S}_3)\rangle$ (K)
$\mathcal{M}_0$	1427	1456	1437
$\mathcal{M}_1$	1475	1478	1441
$\mathcal{M}_2$	1461	1465	1431
Exp.	1380 ± 20	1420 ± 25	1425 ± 25

Table 3
Volume averages computed in the volume of the glove box: amount of fuel consumed ($\dot{m}_{F_1,GB}$ and $\dot{m}_{F_2,GB}$, kg/s), heat released ($\dot{q}_{GB}$, W) and heat dissipated by radiative means ($\dot{q}_{r,GB}$, W).

	$\dot{m}_{F_1,GB}$	$\dot{m}_{F_2,GB}$	$\dot{q}_{GB}$	$\dot{q}_{r,GB}$
$\mathcal{M}_0$	1.1×10^{-2}	2.5×10^{-3}	3.3×10^{5}	1.4×10^{5}
$\mathcal{M}_1$	1.1×10^{-2}	2.3×10^{-3}	3.3×10^{5}	1.6×10^{5}
$\mathcal{M}_2$	1.1×10^{-2}	2.3×10^{-3}	3.4×10^{5}	1.6×10^{5}

major remarks. On the one hand, the internal part of the glove box constitutes a rich atmosphere, and combustion is limited by the entrainment of external oxidizer. On the other hand, whatever the grid under consideration ($\mathcal{M}_0$, $\mathcal{M}_1$, or $\mathcal{M}_2$), almost the same amount of fresh air enters the box, and this leads to the same amount of consumed pyrolysis volatiles, in spite of the lack of turbulence resolution observed for $\mathcal{M}_0$ and, to a lesser extent, for $\mathcal{M}_1$. It is noteworthy that the heat dissipated by radiative transfer $\dot{q}_{r,GB}$ is slightly underestimated with grid $\mathcal{M}_0$ and accounts for approximately 45% of the total heat released in the box, which lies between the radiative fractions of MMA (31%) and Phenol (51%) [33].

5. Conclusions and perspectives

A set of three large-eddy simulations, featuring various levels of grid refinement, has been performed to describe the reactive flow developing during a glove box fire in the phase of maximum heat release rate of the fire scenarios previously studied experimentally at IRSN. To the best of the authors' knowledge, these are the first glove box fire LES documented in the literature. The reliability of the obtained solutions is assessed in two distinct ways. On the one hand, the detailed analysis of the turbulence resolution — based on the calculation of LES quality indexes and turbulence spectra — suggests that a significant part of the inertial range of the turbulent spectrum is resolved for both

the intermediate and most refined computational grids. On the other hand, the computational results obtained on the three computational grids display a satisfactory level of agreement with available experimental measurement of temperature (on the central line of the glove box). This is further supported by the fact that these solutions are all characterized by very similar features, namely accumulation of pyrolysis volatiles inside the box, unsteady entrainment of fresh gases through the lower glove holes and air gaps, combustion of a small fraction of flammable gases, and strong ascending current resulting from the heat release. From a more quantitative point of view, the total rate of combustion, the resulting HRR, and the fraction of heat dissipated by radiative transfer, once averaged over the whole volume of the box, marginally depend on the level of computational refinement. The use of finer grids has only a significant influence on the thickness of the reactive zones, on the depth over which fresh gases are engulfed into the box and on the location of the maxima of reactivity, and therefore heat release and temperature.

The obtained results provide some perspectives that concern the predictions of the maximum heat release in glove box fires by coupling reactive large-eddy simulations in the gas phase with pyrolysis simulations in the condensed phase. Indeed, although the total heat release is correctly estimated at moderate CPU expenses with the coarsest grid, the local distribution of the heat flux on the surface of the pyrolysing panels will be more sensitive to the exact distribution of the reactive zones and, therefore, on the level of grid refinement. In this respect, the flowfields obtained with intermediate and finest grids — characterized by centimetric grid cell sizes — exhibit similar temperature and heat release rate distributions and may thus provide reliable solutions. Unfortunately, the corresponding CPU costs are not compatible with the long-term simulation of pyrolysis processes. Furthermore, it is noteworthy that, with the target of obtaining a reliable estimation of convective and radiative fluxes at the pyrolysing surfaces, these simulations should also meet additional constraints in terms of near-wall refinement in order to correctly resolve the turbulent quantities and the radiative transfer equation. Clearly, an increased CPU time is thus required for an improved estimation of the thermal stress, which is even less suitable for coupled simulations.

In light of these results, reactive large-eddy simulations of glove box fires can be used to improve the estimation of the global heat release and pollutant emission associated in the following ways. Firstly, considering the observed CPU cost of such simulations, long-term gas phase simulations coupled with pyrolysis modelling could be performed provided that (i) the lighter (i.e. coarser) grid is used, (ii) some turbulence forcing is introduced to reproduce the dynamics of the solutions obtained on the finest grids and (iii) suited modelling are applied near the walls to obtain a correct estimation of the fluxes. That is why, considering the ability of reactive LES to describe the flow dynamics of a particular phase in a glove box fire, a second approach may consist in estimating the consequences of the fire (e.g. the possible loss of integrity of the installation, or the release of radioactive material), at a precise step of the fire scenario, given prescribed boundary conditions

in terms of release of pyrolysis volatiles. Finally, such simulations may complement more global modelling strategies used to estimate the temporal evolution of the mass loss rate and heat release rate over the whole duration of a glove box fire, by providing a detailed characterization of the heat transfers towards the blowing surfaces and therefore a reliable description of the thermal stress that is necessarily prescribed in such global models. Keeping this in mind, additional experiments with improved estimations of the boundary conditions and flow quantity measurements would be welcome in order to proceed with a more detailed assessment of the numerical model.

Acknowlegments

This study is a part of the PhD Thesis undertaken by one of us (U. Chikkabikkodu), supported by IRSN. It was granted access to the HPC resources of TGCC under the allocation 2022-A0132B13827 made by GENCI. The authors gratefully acknowledge all these supports.

References

[1] Factory Mutual Research Corporation. Glovebox fire safety — a guide for safe practices in design, protection and operation. Technical Report TID-24236, Norwood, MA, USA, 1967.

[2] U.S. Department of Energy (DOE). The September 1957 rocky flats fire: a guide to record series of the department of energy and its contractor. Technical notes, History Associates Incorporated, 1995.

[3] H. Massie. Glovebox fire at rocky flats environmental technology site. Memorandum, Defense Nuclear Facilities Safety Board, 2003.

[4] P. Zavaleta, M. Coutin, Th. Gélain, J. Lacoue, Ph. March, H. Mastori, H. Najimi, M. Piller, W. Plumecocq, E. Porcheron, M. Sow, and S. Suard. Characterization of the plutonium dioxide airbone release fraction during glove box fires in nuclear fire fabrication and reprocessing plants: presentation of the FIGARO research project and its first outcomes. In *The 30th International Conference on Nuclear Engineering*, Kyoto, Japan, 2023.

[5] M. Coutin and L. Audouin. Glove box fire behaviour in free atmosphere. In *SMIRT 24 15th International Post-Conference Seminar on Fire Safety in Nuclear Power Plants and Installations*, number SA2I-2017-226, Bruges, Belgique, 2017.

[6] P. Zavaleta, S. Charbaut, G. Basso, and L. Audouin. Multiple horizontal cable tray fire in open atmosphere. In Interscience Communications Limited, editor, *Proceedings of the Fire and Materials 2013 Conference*, volume 13, pages 57–68. Interscience Communications Limited, Interscience Communications Limited, 2013.

[7] D. Alibert. *Effet de la sous-oxygénation sur les paramètres de combustion*. PhD thesis, Aix-Marseille Université, 2017.

[8] S. I. Stoliarov, S. Safronava, and R. E. Lyon. Prediction of the burning rates of non-charring polymers. *Combustion and Flame*, 156:1068–1083, 2009.

[9] S. I. Stoliarov, S. Crowley, R. N. Walters, and R. E. Lyon. Prediction of the burning rates of charring polymers. *Combustion and Flame*, 157: 2024–2034, 2010.

[10] Y. Wang, P. Chatterjee, and J. L. De Ris. Large eddy simulation of fire plumes. *Proceedings of the Combustion Institute*, 33(2):2473–2480, 2011.

[11] J. E. Floyd, K. B. Mc Grattan, S. Hostikka, and H. R. Baum. CFD fire simulation using mixture fraction combustion and finite volume radiative heat transfer. *Journal of Fire Protection Engineering*, 13:11–36, 2003.

[12] A. Brown, M. Bruns, M. Gollner, J. Hewson, G. Maragkos, A. Marshall, R. McDermott, B. Merci, T. Rogaume, S. Stoliarov, J. Torero, A. Trouvé, Y. Wang, and E. Weckman. Proceedings of the first workshop organized by the iafss working group on measurement and computation of fire phenomena (macfp). *Fire Safety Journal*, 101:1–17, 2018.

[13] G. Maragkos, T. Beji, and B. Merci. Advances in modelling in CFD simulations of turbulent gaseous pool fires. *Combustion and Flame*, 181: 22–38, 2017.

[14] N. Ren, Y. Wang, S. Vilfayeau, and A. Trouve. Large eddy simulation of turbulent vertical wall fires supplied with gaseous fuel through porous burners. *Combustion and Flame*, 169:194–208, 2016.

[15] G. Boyer. Towards the prediction of the convective and the radiative heat fluxes in turbulent buoyant flames. In *3rd European Symposium on Fire Safety Science*, September 2018.

[16] G. Maragkos and B. Merci. Large eddy simulations of flame extinction in a turbulent line burner. *Fire Safety Journal*, 105:216–226, 2019.

[17] B. F. Magnussen and B. H. Hjertager. On mathematical modeling of turbulent combustion with special emphasis on soot formation and combustion. In *16th Symposium (International) on Combustion*, volume 16, pages 719–729, 1976.

[18] S. Suard, S. Forestier, and S. Vaux. Toward predictive simulations of pool fires in mechanically ventilated compartments. *Fire Safety Journal*, 61:54–64, 2013.

[19] K. B. Mc Grattan, R. J. Mc Dermott, J. Floyd, S. Hostikka, G. Forney, and H. R. Baum. Computational fluid dynamics modelling of fire. *International Journal of Computational Fluid Dynamics*, 26:349–361, 2012.

[20] S. B. Pope. Ten questions concerning the large-eddy simulation of turbulent flows. *New Journal of Physics*, 6(35), 2004.

[21] I. B. Celik, Z. N. Cehreli, and I. Yavuz. Index of Resolution Quality for Large Eddy Simulations. *Journal of Fluids Engineering*, 127(5): 949–958, 09 2005. doi: 10.1115/1.1990201.

[22] Y. Pizzo. *Caractérisation de la flamme de diffusion établie le long d'un combustible solide en convection naturelle par le nombre de transfert de masse*. Engineering sciences, Université de Provence, 2007.

[23] F. Babik. Calif^{3}s-isis v6: Physical modelling. Technical report, IRSN/PSN-RES/SA2I/LIE, 2021. URL https://gforge.irsn.fr/gf/project/isis/docman/Physicalmodelling.

[24] F. Babik. Calif^{3}s-isis v6: Validation. Technical report, IRSN/PSN-RES/SA2I/LIE, 2021. URL https://gforge.irsn.fr/gf/project/isis/docman/Physicalmodelling.

[25] S. Vaux, R. Mehaddi, O. Vauquelin, and F. Candelier. Upward versus downward non-boussinesq turbulent fountains. *Journal of Fluid Mechanics*, 867:374–391, 2019.

[26] S. Vaux, R. Mehaddi, A. Collin, and P. Boulet. Fire plume in a sharply stratified ambient fluid. *Fire Technology*, 57:1969–1986, 2021.

[27] F. Nicoud and F. Ducros. Subgrid-scale stress modelling based on the square of the velocity gradient tensor. *Flow, Turbulence and Combustion*, 62:183–200, 1999.

[28] M.W. Chase Jr. Nist-janaf themochemical tables. *J. Phys. Chem. Ref. Data, Monograph 9*, pages 1–1951, 1998.

[29] T. F. Smith, Z. F. Shen, and J. N. Friedman. Evaluation of coefficients for the weighted sum of gray gases model. *Journal of Heat Transfer (Transactions of the ASME)*, 104:602–608, 1982.

[30] V. Novozhilov. Computational fluid dynamics modeling of compartment fires. *Progress in Energy and Combustion Science*, 27:611–666, 2001.

[31] C.J. Wang, J.X. Wen, Z.B. Chen, and S. Dembele. Predicting radiative characteristics of hydrogen and hydrogen/methane jet fires using FireFOAM. *International Journal of Hydrogen Energy*, 39(35):20560 – 20569, 2014.

[32] G. Montaudo, S. Carroccio, and C. Puglisi. Thermal and themoxidative degradation processes in poly(bisphenol a carbonate). *Journal of Analytical and Applied Pyrolysis*, 64:229–247, 2002.

[33] A. Tewarson. *Generation of Heat and Chemical Compounds in Fires*. National fire proctection association, fourth edition, 2008.

[34] F.H. Harlow and J.E. Welch. Numerical calculations of time-dependent viscous incompressible flow of fluid with a free surface. *Physics of Fluids*, 8, 1965.

[35] F. Boyer, F. Dardalhon, C. Lapuerta, and J.-C. Latché. Stability of a crank-nicolson pressure correction scheme based on staggered discretizations. *International Journal for Numerical Methods in Fluids*, 2013.

[36] J. C. Chai, H. S. Lee, and S. V. Patankar. Finite volume method for radiation heat transfer. *Journal of Thermophysics and Heat Transfer*, 8(3): 419–425, 1994.

[37] P. Sagaut. *Large Eddy Simulation for Incompressible Flows*. Springer, 2001.

[38] E. Ribeiro, R. Henrique, F.and Boukharfane, and A. Mura. Highly-resolved large-eddy simulations of combustion stabilization in a scramjet engine model with cavity flameholder. *Computers and Fluids*, 197:104344, January 2020. URL https://hal.science/hal-02358767.

[39] A. Techer, Y. Moule, G. Lehnasch, and A. Mura. Mixing of fuel jet in supersonic crossflow: estimation of subgrid-scale scalar fluctuations. *AIAA Journal*, 56:465–481, February 2018. URL https://doi.org/10.2514/1.J056251.

[40] S. Welsh and P. Rubini. Three-dimensional simulation of a fire-resistance furnace. In International Association for Fire Safety Science, editor, *Proceedings of the Fifth International Symposium*, 1997.